Geochemical Perspectives Letters

A novel carbon cycle turbulence index identifies environmental and ecological perturbations

Z.-H. Li, Z. Guo, Z.-Q. Chen, S.W. Poulton, Y. Bao, L. Zhao, F.-F. Zhang

Supplementary Information

The Supplementary Information includes:

- The Geochemical and Paleobiology Databases
- Analytical Approaches and Statistical Analysis
- Datum Density *vs.* Bias
- Comparison of Carbon Cycle Perturbations and CTindex Values between the Permian-Triassic Mass Extinction and the Industrial Revolution Period of the Anthropocene
- Tables S-1 and S-2
- Figures S-1 to S-8
- Supplementary Information References

The Geochemical and Paleobiology Databases

The carbon isotope ($\delta^{13}C_{carb}$) dataset through the last one billion years is adapted from Cramer and Jarvis (2020) and collected from other key studies (Xiao *et al.*, 2014; Zhu *et al.*, 2019; Rooney *et al.*, 2020; Westerhold *et al.*, 2020). We note that $\delta^{13}C_{carb}$ data before and after ~650 Ma have markedly different data density (Fig. S-1), with the ~1000 to 650 Ma period having lower density and intervals with no data. However, this feature does not affect the analyses focused on the Phanerozoic.

The Sepkoski database (Sepkoski, 1996) and Paleobiology database (PaleoDB, http://www.paleobiodb.org/, http://fossilworks.org) are employed to calculate biotic extinction rates at the genus level through the Phanerozoic. The former was only used as a comparison in Figure S-2, while the latter was used to run the CT_{index} curves. It should be noted that the raw dataset (PaleoDB) that was used in this study follows Kocsis *et al.* (2019), which was downloaded on May 31, 2019 (https://github.com/divDyn/ddPhanero/raw/master/data/PaleoDB/2019-05-31_paleoDB.RData). Time series were drafted based on the resolution of Stages (Ages), which is the highest resolution of the PaleoDB. Twelve different metrics (Fig. 1b) were set to calculate ER based on three different data treatments, including: raw data, Classical Rarefaction (cr), and Shareholder Quroum Subsampling (sqs). In addition, four different rate calculation methods were employed, including: per capita rates, corrected three-timer rates, gap-filler equations, and second-for-third substitution rates. Kocsis *et al.* (2019) suggested metric, with sqs data treatment and second-for-third substitution rates ('sqs2f3'), should be used as the standard extinction rate trend in this study. The other metrics were used as a necessary contrast to form the error bars in Figure 2.

Analytical Approaches and Statistical Analysis

All mathematical approaches were performed in R (for the PaleoDB) and Matlab (other processes). The original $\delta^{13}C_{carb}$ database has an uneven sample resolution across different intervals. We used an interpolation method to average all densities to 0.02 Ma per point (Fig. S-1), which is employed in Matlab by using the function 'interp1' with method 'Linear'. In particular, the original $\delta^{13}C_{carb}$ database (Westerhold *et al.*, 2020) has a much higher resolution from 0 to 0.5 Ma (~0.005 Ma per point), whilst the resolution from 750 to 2100 A.D. is ~1 year per point. For these higher resolution intervals, we did not lower the resolution to be consistent with more ancient intervals. The CT_{index} value therefore reflects $\delta^{13}C_{carb}$ variability not only on a long-timescale (>10 Ma), but also within a short-timescale (>0.02 Ma). Multiple studies have suggested that $\delta^{13}C_{carb}$ may dominantly reflect the original ocean-atmosphere carbon isotope composition and can sensitively record oscillations across this short-timescale (Bachan *et al.*, 2017), although local restriction, water-mass ageing and authigenic carbonate formation may also affect the isotopic record (Swart, 2008). The CT_{index}, however, weakens the direction or simple magnitude of $\delta^{13}C_{carb}$ excursions and emphasises the possibility of isotopic instability over a predetermined timespan (see sensitivity test in Fig. S-3 for further detail).

The post-interpolation $\delta^{13}C_{carb}$ dataset was used to calculate the CT_{index} according to Equation 1. And the number of datum points within a predetermined τ_{span} should be kept the same to ensure that the calculation of

CT_{index} is not affected by different datum densities across different time periods. Given the fact that differentiation between the parameters τ_{span} and n will significantly shift the output of the calculation, we employed sensitivity analyses of τ_{span} and n to the CT_{index} (Fig. 1), indicating that as both τ_{span} and n increase, the output of the CT_{index} also increases synchronously. However, when the datum density is high (*e.g.*, PTr interval and Cenozoic), there is little deviation when these parameters change (differentiation <10 %). We note here that the parameter τ_{span} plays a more important role in running CT_{index}, and thus dependent on the τ_{span} used, a very different CT_{index} value may be obtained. As shown in Figure S-3, we used some simple 'witches hat' pulses (linear increase followed by linear decline at the same rate), and the time-dependent forcing pulses for $\delta^{13}C_{carb}$ variations are given in Equations S-1-3:

$$\text{Pulse\_1} = [0{:}0.1{:}1.2],\ [0\ 0\ 5\ 0\ 0\ {-5}\ 0\ 0\ 5\ 0\ 0\ 5\ 0] \quad \text{(Eq. S-1)}$$

$$\text{Pulse\_2} = [0\ 0.4\ 0.5\ 0.6\ 1.2],\ [0\ 0\ 5\ 0\ 0] \quad \text{(Eq. S-2)}$$

$$\text{Pulse\_3} = [0\ 0.4\ 0.6\ 0.7\ 0.9\ 1.2],\ [0\ 0\ 7\ 7\ 0\ 0] \quad \text{(Eq. S-3)}$$

where the first vectors are time (in Myrs) and the second vectors are the $\delta^{13}C_{carb}$ values (in ‰). Different τ_{span} values were used for a sensitivity test. Rothman (2017) observed that the duration of the major carbon isotope events through the entire Phanerozoic is approximately limited between 10^4 to 10^6 years. This means that if we employ a longer (larger) τ_{span} (*e.g.*, $\tau_{span} \geq 1$ Ma), the CT_{index} is unable to distinguish individual events, and the CT_{index} curve would represent a mixed signal of adjacent events (Fig. S-3a). This feature is directly evidenced by Pulse_1, which also shows that the CT_{index} is not sensitive to the direction of the carbon isotope excursion. In addition, multiple carbon isotope events have different degrees of offset and duration (simplified as Pulse_2 and Pulse_3). When τ_{span} is greater than the event duration, calculated CT_{index} values and the timing of the CT_{index} perturbation are not accurate (Fig. S-3b). When τ_{span} greatly exceeds the event duration, CT_{index} values approach a straight line with artificially high values (Fig. S-3b). Hence, the τ_{span} value may be greater than the events of relatively small duration (*e.g.*, PTr) and lower than the events of relatively large duration (*e.g.*, SPICE). In this case, we suggest to employ a relatively low τ_{span}, which should be similar to the minimum duration of the events in question (*e.g.*, the duration of the PTr = ~0.06 Ma, and the duration of the PETM = ~0.08 Ma). In this case, a τ_{span} of 0.05 Ma is our recommended standard value, which is greater than the average density (= 0.02 Ma per point) of the $\delta^{13}C_{carb}$ database, but less than the more short-lived intervals of interest. The parameter τ_{span} may still be accurate (but smaller) if the resolution of carbon isotopes is further

improved. For instance, we employ a τ_{span} of 0.0001 Ma (100 years) for our subsequent evaluation of the interval from 700-2100 A.D.

In order to reveal the relationship between CT_{index} and ER, we employed a logistic function to test the data of 41 events (Eq. S-4):

$$P(x) = \frac{K*P_0*e^{rx}}{K+P_0*(e^{rx}-1)} \quad \text{(Eq. S-4)}$$

which calculates the logistic curve (sigmoid curve) and is used to run the logistic regression, where x denotes the CT_{index}, and P(x) denotes the calculated ER. P_0 and K represent background ER and maximum ER values, respectively, and r is a free parameter measuring how fast the curve varies. When the CT_{index} is infinite, ER is equal to K = 1, indicating that all organisms became extinct. A logistic function was fitted to the data (Fig. 2). All the datum points contributing to Figure 3 are listed in Table S-2. When CT_{index} approaches zero indefinitely, the ER = ~0.086.

In order to reveal the similar statistical distribution of the CT_{index} and biotic extinction rates, we employed a log-normal distribution function to test the original databases (Eq. S-5):

$$\varphi\ln(x) = \frac{1}{\sqrt{2\pi}*\delta x}\exp\left(-\frac{(lnx-\mu)^2}{2\delta^2}\right) \quad \text{(Eq. S-5)}$$

$$E(X) = e^{\mu+\delta^2/2} \quad \text{(Eq. S-6)}$$

$$\mathrm{var}(X) = \left(e^{\delta^2}-1\right)*e^{2\mu+\delta^2} \quad \text{(Eq. S-7)}$$

where x denotes that the CT_{index} and generic ER are a random variable. Both μ and σ are free parameters in this distribution function, which are the mean and standard deviation of logarithms of variables, respectively. The mathematic expectation (E(X)) and variance (var(X)) were calculated by Equations S-6 and S-7, respectively. The histograms of the $\delta^{13}C_{carb}$ and ER values fit with log-normal distribution functions (Fig. S-2, Table S-1). The CT_{index} values since the mid-Tonian are divided into two parts: 870-520 Ma and 520-0 Ma. The log-normal best fit curves of the histogram show that the CT_{index} values prior to 520 Ma (E(X) = 0.246) are relatively higher than afterwards (E(X) = 0.168), implying more volatility in the carbon cycle from 860 to 520 Ma. However, we note that there are some $\delta^{13}C_{carb}$ data gaps and this reduces the accuracy of CT_{index} output during the Precambrian period.

Datum Density *vs.* Bias

The $\delta^{13}C_{carb}$ database and PaleoDB covering the entire Phanerozoic were used to calculate the CT_{index} and ER values, respectively. The uneven density distribution in the datasets is a major potential source of the error when calculating both the CT_{index} and the ER. As shown in Fig. S-1b, the density of the $\delta^{13}C_{carb}$ database is lower than 0.05 Ma per point, except for some intervals of high density. Therefore, we have uniformly pre-normalised the density of the $\delta^{13}C_{carb}$ database to 0.02 Ma per point.

The PaleoDB has a different and more complex sampling density to the $\delta^{13}C_{carb}$ database. The density of Stage (or substage) time-bin is lower than that of the $\delta^{13}C_{carb}$ database. Following the Sepkoski (1996) scheme, each stage has three statistical points corresponding to the start, middle and end ages. The calculated ER has the age point set to the middle age of each stage/substage. For instance, the Induan (early Triassic) contains three statistical age points calibrated to 251.9, 251.6 and 251.2 Ma. The ER of the Induan was calculated based on extinction rate data from the middle age point (251.6 Ma), and its value is 0.5, then the ER and its age for the Induan are expressed as [0.5, 251.6]. This differentiation of density causes potential error when calculating the correlation between CT_{index} and ERs (Fig. S-4), because the resolution of this three-statistical-points scheme is much lower than that of the CT_{index} curve, and the major CT_{index} peaks in each stage may not exactly emerge at the three-statistical-points of this stage. For instance, the onset timing of the PTr carbon isotope excursion is ~251.94 Ma, which is apparently not at the three-statistical-points of the Changhsingian. To minimise this bias, we assume that the onset timing of the major extinction events is equal to the onset timing of the major carbon isotope excursion in each stage. In other words, the ER curves have a normalised new timing abscissa, as listed in Table S-2.

In terms of the taxonomic data of the PaleoDB, the uneven collections and/or occurrences will lead to different degrees of data quality between different stages. Specifically, the periods including the early Cambrian, Silurian, and Stages Bashkirian, Kasimovian and Thanetian, are characterised by extremely low collections (red boxes, Fig. S-4a). This will likely make the calculated ERs less reliable, and for these five low-quality data intervals special attention was paid in the following CT_{index} and ER correlation processes.

The PTr and TJ intervals have nearly an order of magnitude higher CT_{index} and ERs than other events, and this can cause the correlation between them to be artificially high. Hence, the CT_{index} and ER values are logarithmic normalised to eliminate the effect of order of magnitude differences in correlation. As shown in Fig. S-5b,

after the logarithmic normalisation, the relationship between the CT_{index} and ER remains highly relevant (R^2 = 0.697, *p* values = 5.21 * 10^{-9}).

Furthermore, positive correlations are also observed between the ER of various clades (phylum or class) and CT_{index} values during these events (Fig. S-5d), where the slopes of the ER-CT_{index} represent the tolerance of animal genera to environmental perturbation, indicating that the precise behavior of each clade is different when the CT_{index} value increases. Specifically, the Cnidaria, Brachiopoda and Cephalopoda suffered more severe extinctions (higher ER-CT_{index} slopes) relative to the Arthropoda, Bivalvia and Gastropoda. This indicates that the Cnidaria were physiologically fragile and more unbuffered, and the other clades were less affected and more physiologically buffered, strengthening observations on the decrease in physiologically unbuffered taxa and increase in physiologically buffered taxa after the PTr extinction (Knoll *et al.*, 2007; Payne *et al.*, 2020).

Comparison of Carbon Cycle Perturbations and CT_{index} Values between the Permian-Triassic Mass Extinction and the Industrial Revolution Period of the Anthropocene

We highlight carbon perturbations and CT_{index} values across two critical periods, represented by the most severe mass extinction of the Phanerozoic, and the last ~300 years before and after the Industrial Revolution (Suess effect). Both periods record high greenhouse gas emissions and pronounced negative excursions in $\delta^{13}C_{carb}$.

In the original $\delta^{13}C_{carb}$ database, data for the PTr period is proxied by the GSSP Meishan section (Burgess *et al.*, 2014). To provide a more detailed case study, we compiled C isotope data for another three well-studied sections around the palaeo-Tethys realm, including: Zal (Iran, Zhang *et al.*, 2018), Bálvány North (Hungary, Schobben *et al.*, 2017), and Wadi Shahha (Arabian, Clarkson *et al.*, 2013). During the PTr, data density is higher than in other geologic intervals, reaching ~10^{-4} Ma per point. Hence, we employed τ_{span} = 0.05 and 0.01 to run the CT_{index}. Fig. S-6 shows that due to the $\delta^{13}C_{carb}$ excursion, the CT_{index} abruptly reaches 1.2 to 1.6 in Meishan, with relatively high values in the other sections, indicating that the huge carbon cycle perturbation was clearly recorded around the entire palaeo-Tethys. With an ER of ~0.81 (Fan *et al.*, 2020), the PTr is distinguished from the other events on a cross plot of ER vs CT_{index} (Fig. 2). However, the datum resolution of the PTr event still has an unbridgeable gap relative to the modern carbon isotope record. Hence, we focus

on an extremely short period containing 11 data points from bed 24e to bed 25 of the Meishan section. This period represents a duration of ~3000 years (Burgess *et al.*, 2014), and is characterised by a significant sharp $\delta^{13}C_{carb}$ excursion, whilst the carbon isotope data were subjected to an Interpolation method to achieve one point per year data resolution (Fig. 3). Then a comparison can be employed between the PTr and the Industrial Revolution period across the same event duration and τ_{span}.

In terms of the Industrial Revolution period, we compiled $\delta^{13}CO_2$ data from 700 to 2100 A.D. (Rubino *et al.*, 2013; Bauska *et al.*, 2015; Graven *et al.*, 2020). For the geologic record we used carbonate carbon isotopes, but for the Industrial Revolution period we used atmospheric CO_2 carbon isotopes. While the carbon isotope signatures from these different sources have different triggering mechanisms and observations, they should result in only a minor difference in the final CT_{index} values. For example, for coral carbon isotope records around the world, the average declining rate = -0.022 ‰ per year from 1960 to 2000 A.D. (Liu *et al.*, 2021); for the globally averaged $\delta^{13}C$-DIC (dissolved inorganic carbon) at the sea-surface, the declining rate = -0.013 ‰ per year from 1960 to 2000 A.D. (Kwon *et al.*, 2021); for $\delta^{13}CO_2$ in ice core the declining rate = -0.025 ‰ per year from 1960 to 2000 A.D. (Rubino *et al.*, 2013). These carbon carriers all record the 'Suess effect', which is a dilution effect whereby burning of fossil fuels increases $^{12}CO_2$ at a faster relative rate than $^{13}CO_2$ and $^{14}CO_2$ (Suess, 1955). For the $\delta^{13}C$ composition of CH_4 in Antarctica ice core, the increasing rate = 0.024 ‰ per year from 1960 to 2000 A.D. (Mischler *et al.*, 2009), which is caused by biomass burning being closely related to the agricultural source scales and population. The calculated CT_{index} curves for these four carbon carriers are plotted in Figure S-7. All four carriers show peaks of the same order of magnitude as during the PTr. It should be noted that the $\delta^{13}C$-coral records (orange lines) and $\delta^{13}CO_2$ (yellow lines) have totally different carbon isotopic values and shifts, but they show nearly the same CT_{index} curves, demonstrating that from the point of view of the CT_{index}, the $\delta^{13}CO_2$ record can be directly compared to the $\delta^{13}C$-coral record, and hence the palaeo-$\delta^{13}C_{carb}$ record.

The near future data in Figure S-8 were predicted by using six scenarios based on the shared socioeconomic pathways (SSPs) from the 6th Coupled Model Intercomparing Project (CMIP6) (Graven *et al.*, 2020), with each scenario having a profound influence on the determination of the CT_{index}. If $\delta^{13}CO_2$ peaks in the near future and falls back quickly, the CT_{index} will be limited to a much lower value, but if $\delta^{13}CO_2$ keeps falling, the 'Suess effect' may create a larger and sharper carbon isotope excursion than the PTr, resulting in a major CT_{index} peak. A τ_{span} of 0.05 Ma was used to calculate the Industrial Revolution period CT_{index} data, in order to compare to the deep-time data resolution. However, as discussed in relation to the τ_{span} sensitivity test (Fig.

S-3), when τ_{span} is a significantly larger than the duration of the event, the CT_{index} approaches a straight line and represents a mixed signal within the time span. Hence, we keep all the variables (or parameters) at the same values to compare the PTr and Industrial Revolution periods. Since the time resolution of the Industrial Revolution is much higher than that of the PTr, we employed τ_{span} = 0.0001 Ma (100 year) and n = 1 to run the CT_{index} of both PTr (251.94 to 251.942 Ma) and Industrial Revolution (1700 to 2100 A.D.) periods, and the resolution of the datasets were set to equal to one point per one year by employing the function 'interp1'with method 'Linear' in Matlab.

Supplementary Tables

Table S-1 The best-fit parameters of the log-normal function fitted to the histograms.

	CT_index		Extinction rate	
	520 - 860 Ma	0 - 520 Ma	Sepkoski (1996)	Kocsis *et al*. (2019)
μ	-3.563	-3.228	-1.906	-1.998
δ	1.887	1.912	0.837	1.013
E(X)	0.168	0.246	0.211	0.226
var(X)	0.964	2.284	0.045	0.092

Table S-2 Event names, event intervals (stages and ages) and data used to construct Figures 2 and S-5. B. = background, representing stabilised and diversification intervals with extremely low ER and CT_{index} values. These events are timed by biostratigraphy with reference to the Geologic Time Scale (Cramer and Jarvis 2020). The fourth column contains the average CT_{index} values during the event intervals. Extinction rates after Kocsis *et al.* (2019) are proportionally normalised to a range of 0 to 1, the sixth column is derived from the method 'sqs2f3'. ER_Diff_Min. and Max. represent the minimum and maximum values under all the ER calculation methods in Kocsis *et al.* (2019), respectively. ER_error_bar_N. = (ER_sqs2f3 - ER_Diff_Min.), ER_error_bar_P. = (ER_Diff_Max - ER_sqs2f3.) Neg. = negative, Pos. = positive. ER of different phylum is derived from the method 'sqs2f3'.

Events	Age (Ma)	Stages	CT_index (‰)	CT_error bar	ER_sqs2f3 (normalised)	ER_Diff		ER_error_bar		Extinction_rate_different_phylum					
						Min.	Max.	Neg.	Pos.	Cnidaria	Brachiopoda	Cephalopoda	Arthropoda	Bivalvia	Gastropoda
1900 - 2100 A.D.		After Suess effect	0.4 - 1.5	0.06											
750 - 1900 A.D.		Before Suess effect	< 0.1	0.06											
0 - 0.0117 Ma		Holocene	0.23	0.06											
Pli	2.6 - 3.6	Late Pliocene	0.11	0.06	0.19	0.10	0.32	0.09	0.14	0.16	0.06		0.19	0.12	0.18
B._Tor	9 - 10	Tortonian	0.04	0.06	0.02	0.02	0.13	0.00	0.11	0.10	-0.01		0.16	0.00	-0.03
B._Lan	13.8 - 13.9	Langhian	0.03	0.06	0.05	0.00	0.12	0.05	0.07	0.00	0.07		0.08	0.01	0.06
PrOM	36.6 - 36.7	Priabonian	0.12	0.06	0.14	0.06	0.18	0.08	0.05	0.11	0.29		0.35	0.08	0.11
B._ETM2	53.54 - 53.62	Ypresian	0.10	0.06	0.05	0.03	0.09	0.01	0.05	0.07	0.09	0.00	0.26	0.02	-0.01
PETM	55.73 - 56.01	Thanetian - Ypresian Tran.	0.33	0.06	0.07	0.06	0.20	0.01	0.13	0.12	0.26	0.06	0.01	0.01	0.06
KPg	65.975 - 66.0	Maastrichtian - Danian Tran.	0.13	0.06	0.28	0.13	0.41	0.15	0.13	0.34	0.34		0.14	0.35	0.22
OAE2	94.46 - 94.54	Cenomanian-Turonian Tran.	0.26	0.06	0.22	0.06	0.31	0.16	0.09	0.24	0.43	0.47	0.21	0.11	0.10
OAE1a	120.1 - 120.2	Aptian	0.19	0.06	0.19	0.07	0.27	0.13	0.08	0.10	0.12	0.25	0.13	0.06	0.05
Kim	149.8 - 149.86	Late Kimmeridgian	0.14	0.06	0.15	0.06	0.22	0.09	0.07	0.01	0.36	0.31	0.39	0.10	0.11
PToBE & TOAE	182 - 185	Pliensbachian - Toarcian Tran.	0.24	0.06	0.19	0.05	0.22	0.14	0.03	0.44	0.27	0.39	0.01	0.09	0.13
TJ	201.25 - 201.3	Rhaetian - Hettangian Tran.	1.02	0.06	0.51	0.18	0.69	0.33	0.18	0.65	0.30	0.99	0.27	0.14	0.24
Nor	215.62 - 215.74	Norian	0.40	0.06	0.28	0.10	0.34	0.18	0.06	0.17	0.32	0.35	-0.05	0.25	0.18
CPE	234.4 - 234.46	Mid - Carnian	0.22	0.06	0.20	0.13	0.29	0.08	0.09	0.17	0.31	0.31	0.20	0.06	0.11
B._An	242 - 243	Late Anisian	0.02	0.06	0.02	0.01	0.11	0.02	0.09		0.01	0.11	0.08	0.06	0.01

Ind	251.42 - 251.52	Induan	0.39	0.06	0.26	0.07	0.40	0.19	0.14			-0.02	0.06	0.04	0.12
PTr	251.941 - 251.88	Changhsingian - Induan Tran.	1.16	0.06	0.81	0.34	0.89	0.47	0.08		0.95	0.63	0.26	0.74	0.57
Cap	260.5 - 261	Mid - Capitanian	0.51	0.06	0.20	0.13	0.27	0.07	0.07	0.16	0.17	0.34	0.08	0.15	0.07
B._Sak	291.5 - 292.5	Sakmarian	0.05	0.06	0.01	0.01	0.11	0.00	0.11	0.07	0.00	0.24	-0.09	-0.03	0.01
B._Gzh	300 - 301	Gzhelian	0.03	0.06	0.05	0.03	0.15	0.02	0.11	0.06	-0.01	0.15	0.06	-0.08	0.13
VS	335.5 - 335.7	Visean - Serpukhovian Tran.	0.31	0.06	0.22	0.09	0.34	0.13	0.11	0.25	0.14	0.24	0.40	0.05	0.07
Hangenberg	359.2 - 359.7	Famennian - Tourisian Tran.	0.62	0.06	0.38	0.14	0.40	0.24	0.02	0.43	0.36	0.36	0.32	0.16	0.19
FF	375 - 372	Frasnian	0.20	0.06	0.16	0.12	0.35	0.04	0.19	0.37	0.13	0.13	0.14	0.12	0.04
GF	379 - 380	Givetian - Frasnian Tran.	0.43	0.06	0.23	0.16	0.33	0.07	0.10	0.44	0.13	0.34	0.41	0.07	0.14
Pri	419 - 419.5	Late Pridoli	0.22	0.06	0.13	0.09	0.19	0.05	0.06	0.04	0.13	0.02	0.15	0.15	0.02
Sil_Lau	423.1 - 423.5	Ludfordian	0.68	0.06	0.05	0.02	0.09	0.02	0.05	0.01	0.05	0.02	0.03	0.05	0.08
Sil_Mulde	427.66 - 428.32	Homerian	0.66	0.06	0.07	0.06	0.16	0.02	0.09	0.02	0.11		0.14	0.04	-0.03
Sil_Ireviken	431.72 - 431.84	Sheinwoodian	0.61	0.06	0.10	0.07	0.14	0.02	0.04	0.10	0.08		0.03	0.16	0.00
B._Rhu	441 - 443	Rhuddanian	0.11	0.06	0.05	0.05	0.16	0.00	0.11	0.03	0.14	-0.03	0.15	0.01	0.00
Ord_2	444.56 - 444.74	Hirntian	0.48	0.06	0.23	0.13	0.37	0.10	0.14	0.14	0.06	0.29	0.27	0.14	0.19
Ord_1	452.42 - 452.48	Early Katian	0.60	0.06	0.40	0.16	0.48	0.24	0.09	0.28	0.28	0.28	0.35	0.10	0.15
B._Dar	460 - 465	Darriwilian	0.02	0.06	0.04	0.00	0.22	0.04	0.18		0.14	0.01	0.13	-0.01	0.09
TSICE	481.9 - 482.5	Tremadocian	0.28	0.06	0.59	0.39	0.64	0.20	0.05		0.47	0.53	0.81		0.59
JiangS	494.2 - 494.4	Paibian - Jiangshanian Tran.	0.15	0.06	0.44	0.23	0.61	0.22	0.16		0.22		0.73		
SPICE	496.42 - 496.5	Paibian	0.17	0.06	0.12	0.11	0.26	0.01	0.14		0.06		0.08		
Cam_7	497.1 - 497.2	Late Guzhangian	0.12	0.06	0.64	0.32	0.90	0.31	0.26		0.61		0.97		
Cam_6	503.7 - 504.2	Drumian	0.12	0.06	0.69	0.30	0.75	0.40	0.06		0.16		0.81		
Cam_5	508.7 - 508.9	Wulian	0.13	0.06	0.45	0.31	0.57	0.14	0.12		0.19		0.87		
Cam_4	514.12 - 514.34	Cambrian Age 4	0.14	0.06	0.47	0.39	0.63	0.08	0.16		0.46		0.14		
Cam_3	517.82 - 518	Cambrian Age 3	0.18	0.06	0.36	0.21	0.39	0.15	0.03		0.42				
Cam_2	521 - 529	Cambrian Age 2	0.41	0.06	0.19	0.18	0.34	0.01	0.15		0.19				

Supplementary Figures

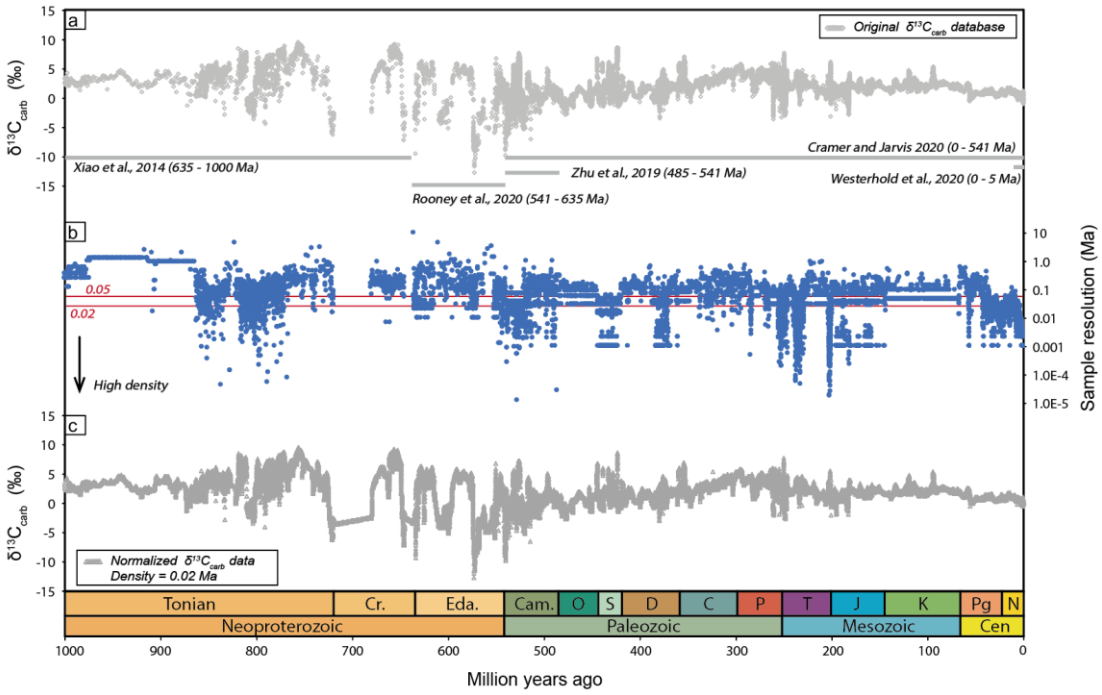

Figure S-1 (**a)** Variation in $\delta^{13}C_{carb}$ through the last 1 billion years. Data sources are indicated by lateral bars showing chronostratigraphic intervals. **(b)** Sample resolution over the one-billion-year interval. **(c)** The normalised $\delta^{13}C_{carb}$ dataset, where the function 'interp1'with method 'Linear' in Matlab was used to uniformly change the data density to 0.02 Ma.

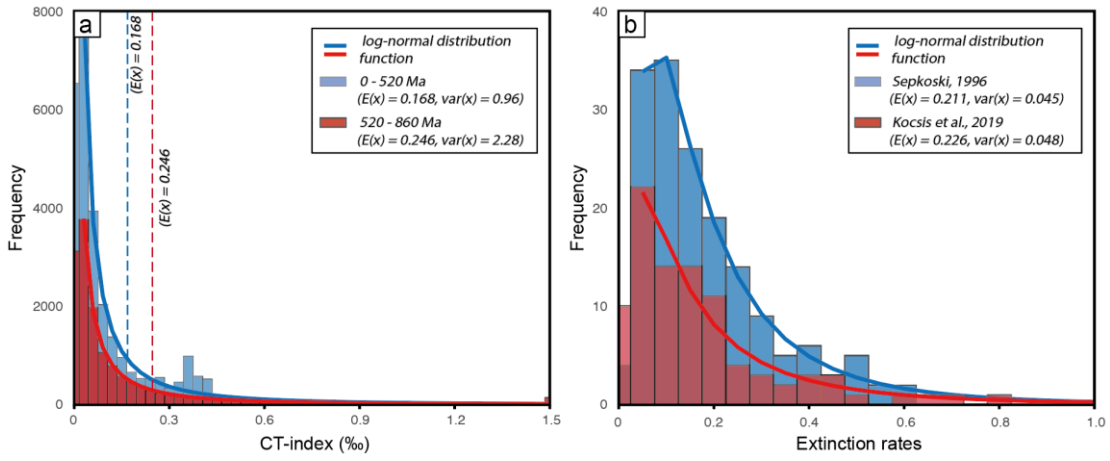

Figure S-2 Histograms and best fit curves of the log-normal function relative to: a. CT_{index} values (0 to 1000 Ma); b. calculated extinction rates (Sepkoski, 1996; Kocsis *et al.*, 2019). E(x) and var(x) represent the mathematical expectation and variation of the dataset x, respectively.

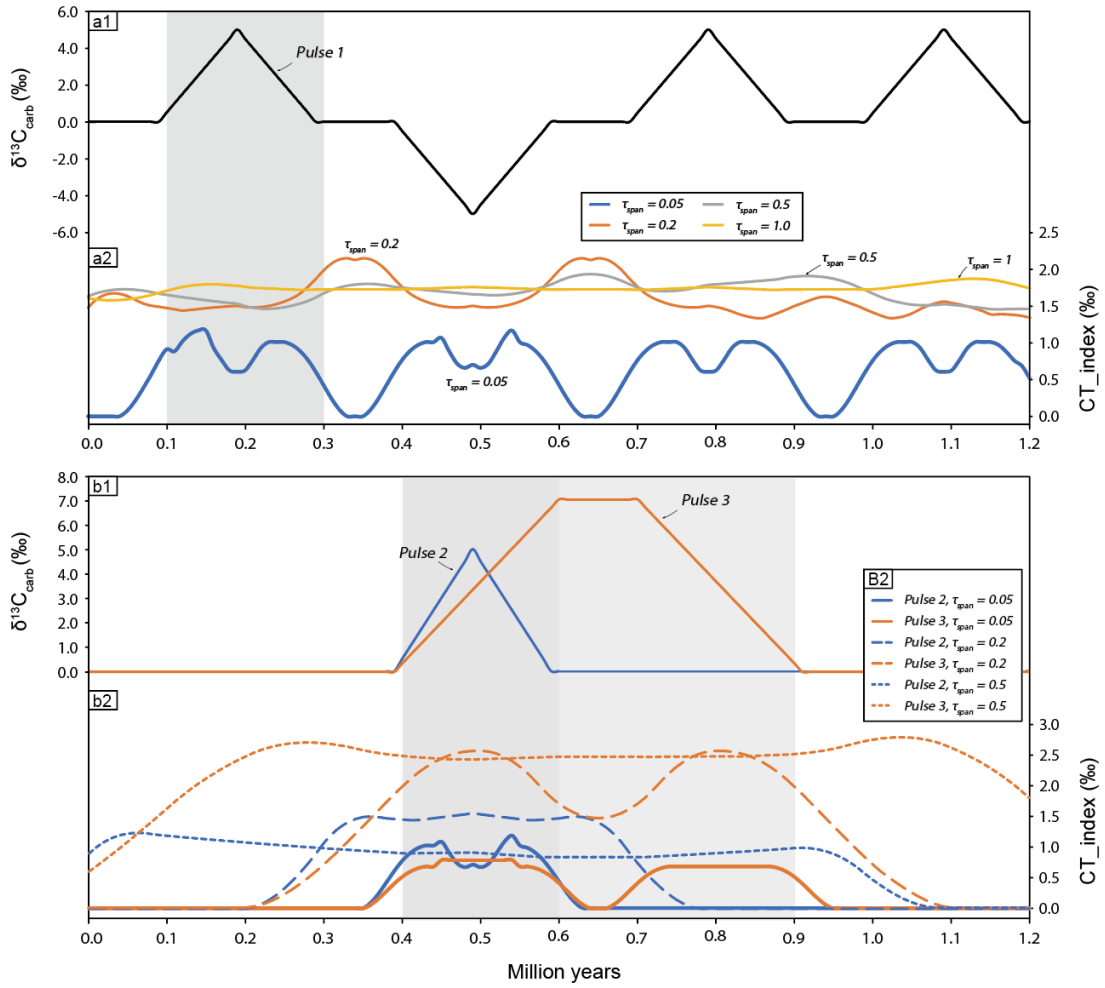

Figure S-3 Sensitivity test for parameter τ_{span}. **(a1-2)** Pulse 1 with four different τ_{span} values (0.05, 0.2, 0.5, 1 Ma). The CT_{index} is not sensitive to the direction of the carbon isotope excursions, and a longer τ_{span} obscures individual events and gives unrealistically high CT_{index} values. **(b1-2)** Pulse 2 and 3, with three different τ_{span} values (0.05, 0.2, 0.5 Ma). The relationship between the duration of the events and the τ_{span} has a profound effect on calculated CT_{index} values.

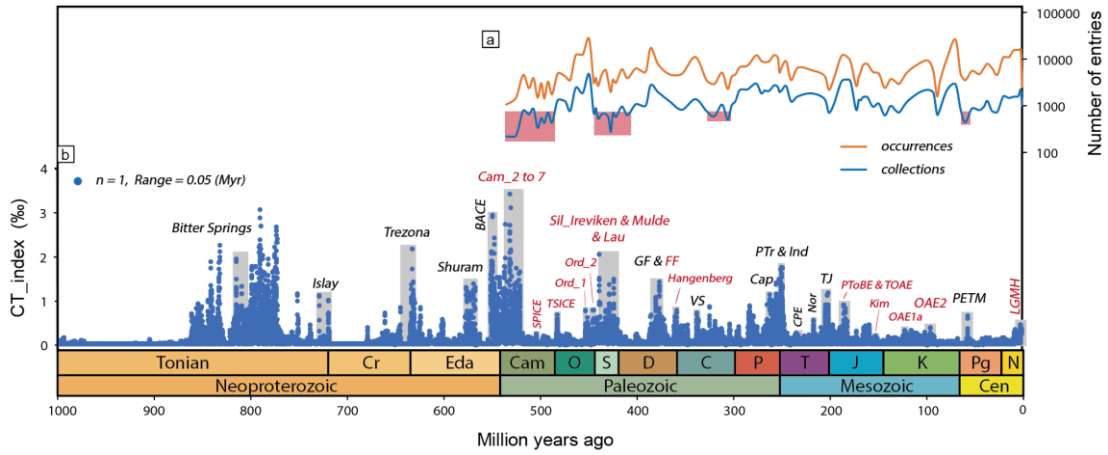

Figure S-4 (a) Occurrences and collections of the Paleobiology database through the Phanerozoic. The red boxes represent the period with extremely low collections including: Cambrian, the Silurian, and stages Bashkirian, Kasimovian and Thanetian. **(b)** CT_{index} peaks and their correspondent $\delta^{13}C_{carb}$ events over the last 1,000 Myr. All CT_{index} peaks correspond to extreme $\delta^{13}C_{carb}$ events, documenting either positive or negative excursions. See Table S-2 for event names. Black and red marks represent negative and positive $\delta^{13}C_{carb}$ excursions, respectively.

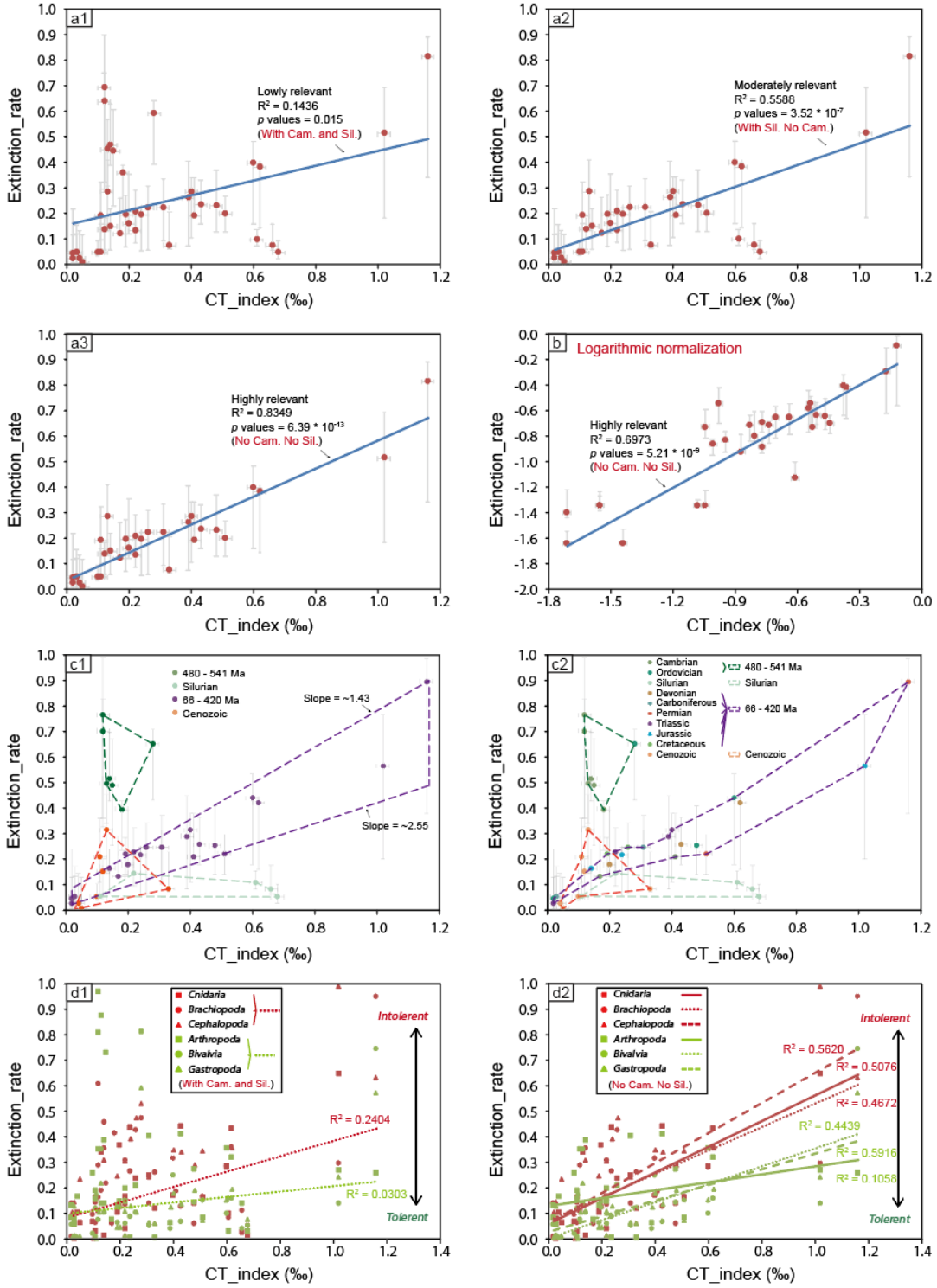

Figure S-5 Cross-plots of the CT_{index} and ER, and their correlations **(a1)** with Cambrian and Silurian data, **(a2)** with Silurian and without Cambrian data, and **(a3)** without Cambrian and Silurian data. **(b)** The CT_{index} and ER values are logarithmic normalised to eliminate the effect of order of magnitude differences in correlation. This accounts for the effect of extremely high values during the PTr and TJ. **(c1-2)** Cross-plots of the CT_{index} and ER for different time intervals. Nearly all the data points fall within the purple zones, with the exception of the Cambrian, Silurian and Cenozoic. (d1-

2) Cross-plots of the CT_{index} and ER for different phyla. The higher the ER/CT_{index} slope, the more intolerant the phylum was during the extinction events.

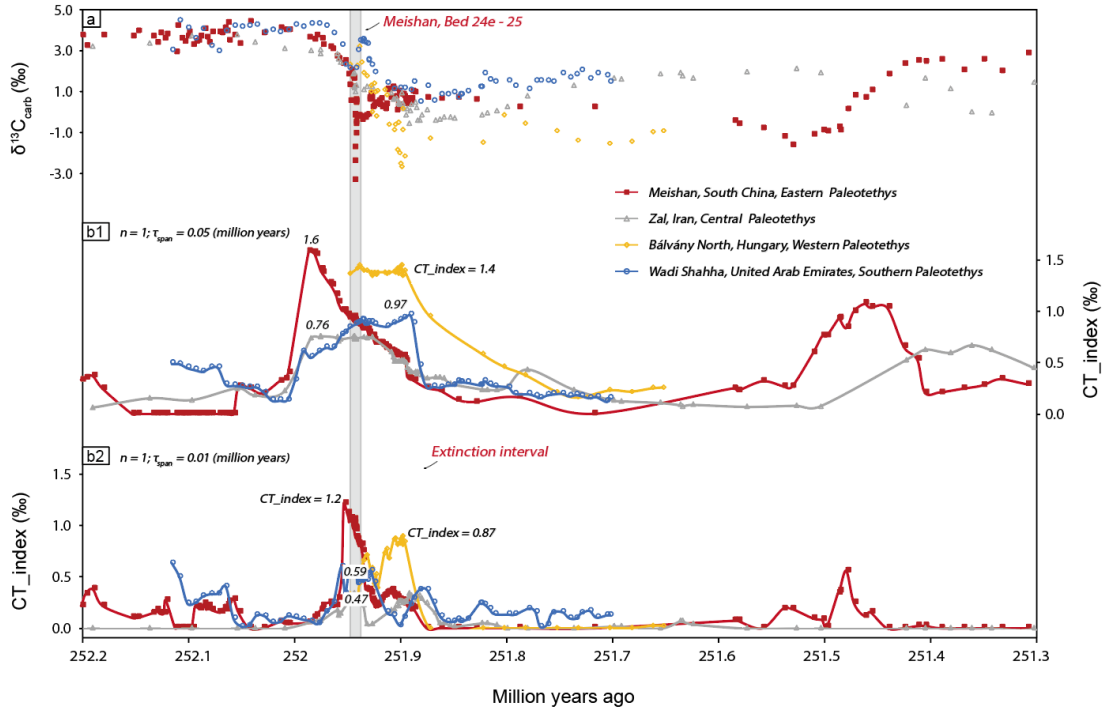

Figure S-6 (a) $\delta^{13}C_{carb}$ data for the Permian-Triassic transition from 252.2 to 251.3 Ma. Data sources: Meishan (Burgess *et al.*, 2014), Zal (Zhang *et al.*, 2018), Bálvány North (Schobben *et al.*, 2017), Wadi Shahha (Clarkson *et al.*, 2013). **(b1-2)** CT_{index} for the $\delta^{13}CO_2$ curves, where parameter n = 1, and r was set equal to 0.05 **(b1)** and 0.01 **(b2)**.

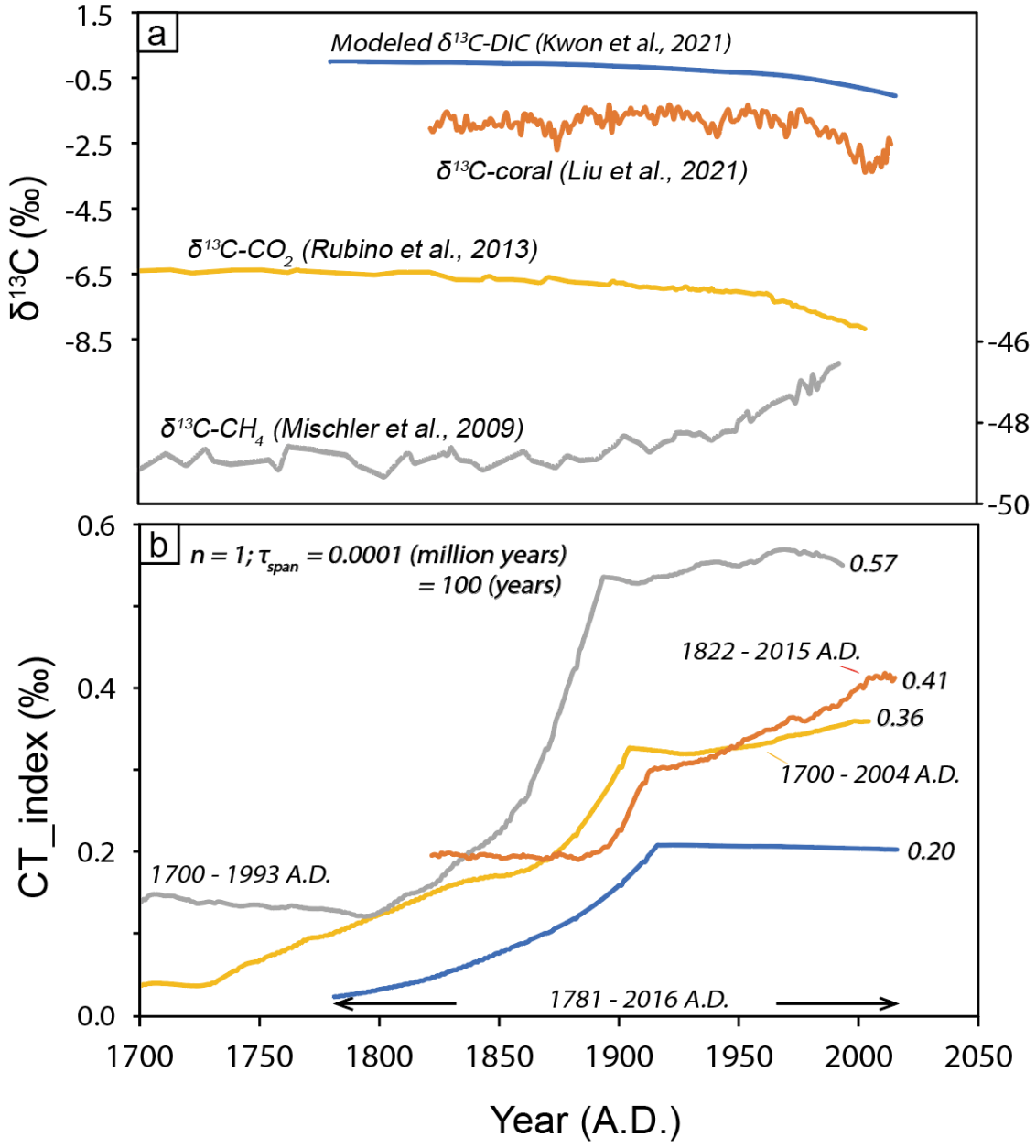

Figure S-7 (a) Carbon isotope trajectories for ocean surface dissolved inorganic carbon (DIC), coral from the northern South China sea, CO_2 from air bubbles trapped in continental ice, and CH_4 in Antarctica ice core. **(b)** Calculated CT_{index} for these datasets. Data sources, the time interval of each dataset, and the CT_{index} values are marked on the figure.

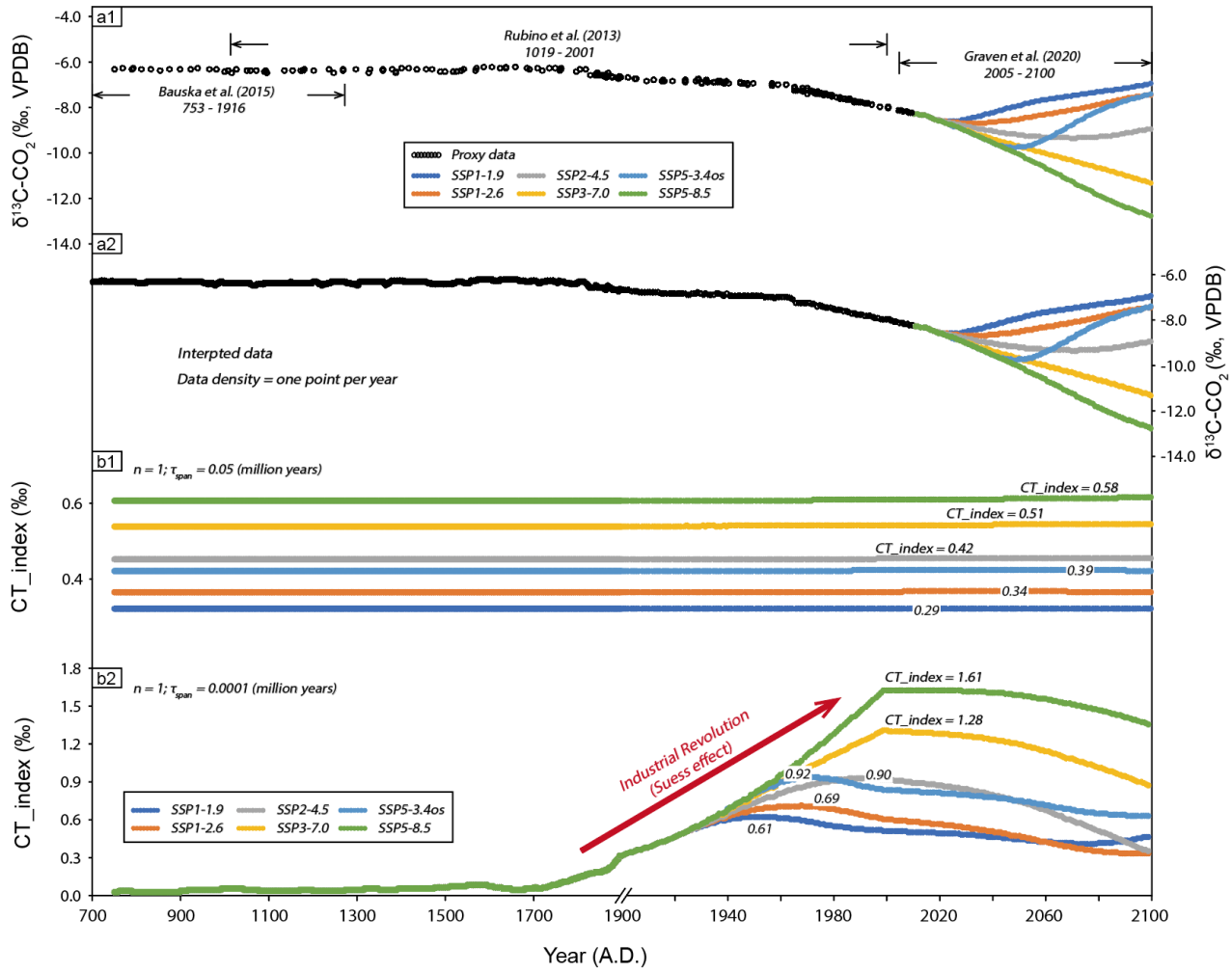

Figure S-8 (a) Observed $\delta^{13}CO_2$ for 750 to 2015 A.D., and simulated $\delta^{13}CO_2$ for 2015 to 2100 A.D. for the six SSP-based CMIP6 ScenarioMIP scenarios (after Graven *et al.*, 2020). Data sources are indicated by lateral bars. **(b1-2)** CT_{index} of the $\delta^{13}CO_2$ curves, where parameter n = 1, and r was set equal to 0.05 **(b1)** and 0.0001 **(b2)**, respectively. A.D. = Anno Domini.

Supplementary Information References

Bachan, A., Lau, K. V., Saltzman, M.R., Thomas, E., Kump, L.R., Payne, J.L. (2017) American journal of science: A model for the decrease in amplitude of carbon isotope excursions across the phanerozoic. *American Journal of Science* 317, 641–676.

Bauska, T.K., Joos, F., Mix, A.C., Roth, R., Ahn, J., Brook, E.J. (2015) Links between atmospheric carbon dioxide, the land carbon reservoir and climate over the past millennium. *Nature Geoscience* 8, 383–387.

Burgess, S.D., Bowring, S., Shen, S.Z. (2014) High-precision timeline for Earth's most severe extinction. *Proceedings of the National Academy of Sciences of the United States of America* 111, 3316–3321.

Clarkson, M.O., Richoz, S., Wood, R.A., Maurer, F., Krystyn, L., McGurty, D.J., Astratti, D. (2013) A new high-resolution δ13C record for the Early Triassic: Insights from the Arabian Platform. *Gondwana Research*. International Association for Gondwana Research 24, 233–242.

Cramer, B.D., Jarvis, I. (2020) Chapter 11 - Carbon Isotope Stratigraphy. In: Gradstein, F.M., Ogg, J.G., Schmitz, M.D., Ogg, G.M. (Eds.) *The Geologic Time Scale 2020*. Elsevier, Amsterdam, 309–343, doi: 10.1016/B978-0- 12-824360-2.00011-5.

Fan, J.X., Shen, S.Z., Erwin, D.H., Sadler, P.M., Macleod, N., Cheng, Q.M., Hou, X.D., Yang, J., Wang, X.D., Wang, Y., Zhang, H., Chen, X., Li, G.X., Zhang, Y.C., Shi, Y.K., Yuan, D.X., Chen, Q., Zhang, L.N., Li, C., Zhao, Y.Y. (2020) A high-resolution summary of Cambrian to Early Triassic marine invertebrate biodiversity. *Science* 367, 272–277.

Graven, H., Keeling, R.F., Rogelj, J. (2020) Changes to Carbon Isotopes in Atmospheric CO2 Over the Industrial Era and Into the Future. *Global Biogeochemical Cycles* 34, 1–21.

Knoll, A.H., Bambach, R.K., Payne, J.L., Pruss, S., Fischer, W.W. (2007) Paleophysiology and end-Permian mass extinction. *Earth and Planetary Science Letters* 256, 295–313.

Kocsis, A.T., Reddin, C.J., Alroy, J., Kiessling, W. (2019) The r package divDyn for quantifying diversity dynamics using fossil sampling data. *Methods in Ecology and Evolution* 10, 735-743.

Kwon, E.Y., DeVries, T., Galbraith, E.D., Hwang, J., Kim, G., Timmermann, A. (2021) Stable Carbon Isotopes Suggest Large Terrestrial Carbon Inputs to the Global Ocean. *Global Biogeochemical Cycles* 35, 1–25.

Liu, X., Deng, W., Cui, H., Chen, X., Cai, G., Zeng, T., Wei, G. (2021) Change of coral carbon isotopic response to anthropogenic Suess effect since around 2000s. *Marine Environmental Research* 168, 105328.

Mischler, J.A., Sowers, T.A., Alley, R.B., Battle, M., McConnell, J.R., Mitchell, L., Popp, T., Sofen, E., Spencer, M.K. (2009) Carbon and hydrogen isotopic composition of methane over the last 1000 years. *Global Biogeochemical Cycles* 23, 1–13.

Payne, J.L., Bachan, A., Heim, N.A., Hull, P.M., Knope, M.L. (2020) The evolution of complex life and the stabilization of the Earth system. *Interface Focus* 10, 20190106.

Rothman, D.H. (2017) Thresholds of catastrophe in the Earth system. *Science Advances* 3, e1700906.

Rooney, A.D., Cantine, M.D., Bergmann, K.D., Gómez-Pérez, I., Baloushi, B. Al, Boag, T.H., Busch, J.F., Sperling, E.A., Strauss, J.V. (2020) Calibrating the coevolution of Ediacaran life and environment. *Proceedings of the National Academy of Sciences of the United States of America* 117, 16824–16830.

Rubino, M., Etheridge, D.M., Trudinger, C.M., Allison, C.E., Battle, M.O., Langenfelds, R.L., Steele, L.P., Curran, M., Bender, M., White, J.W.C., Jenk, T.M., Blunier, T., Francey, R.J. (2013) A revised 1000 year atmospheric δ13 C-CO2 record from Law Dome and South Pole, Antarctica. *Journal of Geophysical Research Atmospheres* 118, 8482–8499.

Schobben, M., Stebbins, A., Algeo, T.J., Strauss, H., Leda, L., Haas, J., Struck, U., Korn, D., Korte, C. (2017) Volatile earliest Triassic sulfur cycle: A consequence of persistent low seawater sulfate concentrations and a high sulfur cycle turnover rate? *Palaeogeography, Palaeoclimatology, Palaeoecology* 486, 74–85.

Sepkoski, J.J. (1996) Patterns of Phanerozoic Extinction: a Perspective from Global Data Bases. *Global Events and Event Stratigraphy in the Phanerozoic* 35–51.

Suess, H.E. (1955) Radiocarbon concentration in modern wood. *Science* 122, 415–417.

Swart, P.K. (2008) Global synchronous changes in the carbon isotopic composition of carbonate sediments unrelated to changes in the global carbon cycle. *Proceedings of the National Academy of Sciences of the United States of America* 105, 13741–13745.

Westerhold, T., Marwan, N., Drury, A.J., Liebrand, D., Agnini, C., Anagnostou, E., Barnet, J.S.K., Bohaty, S.M., Vleeschouwer, D.D., Florindo, F., Frederichs, T., Hodell, D.A., Holbourn, A.E., Kroon, D., Lauretano, V., Littler, K., Lourens, L.J., Lyle, M., Palike, H., Rohl, U., Tian, J., Wilkens, R.H., Wilson, P.A., Zachos, J. (2020) An astronomically dated record of Earth's climate and its predictability over the last 66 million years. *Science* 369, 1383–1388.

Xiao, S., Shen, B., Tang, Q., Kaufman, A.J., Yuan, X., Li, J., Qian, M. (2014) Biostratigraphic and chemostratigraphic constraints on the age of early Neoproterozoic carbonate successions in North China. *Precambrian Research*, 246, 208–225.

Zhang, F.F., Romaniello, S.J., Algeo, T.J., Lau, K.V., Clapham, M.E., Richoz, S., Herrmann, A.D., Smith, H., Horacek, M., Anbar, A.D. (2018) Multiple episodes of extensive marine anoxia linked to global warming and continental weathering following the latest Permian mass extinction. *Science Advances* 4, e1602921.

Zhu, M., Yang, A., Yuan, J., Li, G., Zhang, J., Zhao, F., Ahn, S.Y., Miao, L. (2019) Cambrian integrative stratigraphy and timescale of China. *Science China Earth Sciences* 62, 25–60.